

Cheap and scalable synthesis of α -Fe₂O₃ multi-shelled hollow spheres as high-performance anode materials for lithium ion batteries†

Cite this: DOI: 10.1039/c3cc43867h

Received 23rd May 2013,
Accepted 30th July 2013

DOI: 10.1039/c3cc43867h

www.rsc.org/chemcomm

Liang Zhou,^a Hongyi Xu,^b Hongwei Zhang,^a Jie Yang,^a Sandy B. Hartono,^a
Kun Qian,^a Jin Zou^{bc} and Chengzhong Yu^{*a}

Delicate α -Fe₂O₃ multi-shelled hollow spheres have been prepared by a simple and scalable spray drying method followed by annealing in air. The resulting material shows high specific capacity, good cycling stability, and excellent rate performance in lithium ion battery applications.

Hollow structures, a unique family of materials with low density, high surface area, and shell permeability, have attracted tremendous attention in drug delivery, gas sensors, as well as energy storage and conversion.¹ Recently, efforts have been devoted to the rational design of multi-shelled hollow spheres (MSHSs) due to both their aesthetic beauty and the opportunity for further tailoring of physical–chemical properties by manipulating their shell structures.² The most popular approach for the fabrication of MSHSs involves the shell-by-shell deposition of desired materials onto sacrificial templates followed by selective template removal. Hard templates, such as monodispersed polymers,³ silica,⁴ carbon,⁵ and metal–metal oxide nanoparticles,⁶ or soft ones, such as micelles,⁷ have been widely utilized as the sacrificial templates. However, the templating approach is usually tedious and costly; and the more complex the target structure, the more complicated the synthesis procedure.⁸ Therefore, it is highly desirable to develop a simple and scalable method for the fabrication of MSHSs.

Hematite (α -Fe₂O₃), the most stable form of iron oxide, has been extensively studied as anode material for lithium ion batteries (LIBs) due to its high theoretical capacity (1007 mA h g⁻¹), abundance, low cost, and environmentally benign nature.⁹ Despite these advantages, the application of α -Fe₂O₃ in LIBs is still hampered by the large volume variation during lithiation–delithiation (~96%), which causes the notorious problem of pulverization and the subsequent

capacity fading.^{9b} To alleviate the volume change issue, several strategies have been proposed. One effective strategy is designing unique nanostructures, such as hollow structures and porous materials,^{9a,10} in which the free space in the nanostructures is used to partially accommodate the huge volume change. Another commonly used approach is fabricating nanocomposites of carbon and α -Fe₂O₃, where the carbon acts as a buffer layer.^{10a,11} However, the synthesis of state-of-the-art α -Fe₂O₃ based nanostructures and nanocomposites usually involves expensive sacrificial templates, cumbersome multisteps, or time-consuming solvothermal reactions in autoclaves. Thus, the development of simple, economic, and scalable approaches to produce α -Fe₂O₃ anode materials with satisfactory capacity and rate capability becomes essential.

Spray drying is a widely applied technology in chemical, pharmaceutical, and food industries. It enables simple, continuous, and scalable production of fine particles. However, the application of the spray-drying technique in the preparation of electrode materials with delicate structures and high performance has received little attention. To the best of our knowledge, there is no report on the synthesis of α -Fe₂O₃ multi-shelled hollow spheres by spray drying.

Herein, we develop a facile method for the low-cost and scalable synthesis of α -Fe₂O₃ MSHSs by spray drying. The synthesis involves simply spray drying two cheap precursors, iron nitrate and sucrose, followed by annealing in air. More importantly, the resultant α -Fe₂O₃ MSHSs exhibit high specific capacity, excellent rate capability and good cycling stability. Our method has the potential to be generally applied to the synthesis of other inorganic hollow structures with low cost and high performance.

Fig. 1 illustrates the synthesis of α -Fe₂O₃ MSHSs schematically. The first step involves the preparation of iron nitrate–sucrose composite microspheres (Fig. S1, ESI†) by spray drying; while the second step is annealing the composite spheres in air (Fig. S2, ESI†). The non-equilibrium heat treatment induced heterogeneous contraction^{2c,12} dominates the second step and is responsible for the formation of the α -Fe₂O₃ MSHSs. More specifically, the iron nitrate–sucrose microspheres are not homogeneously heated during the annealing; instead, there exists a temperature gradient (ΔT) along the radial direction. The ΔT leads to the first formation of a α -Fe₂O₃ shell at the surface of the composite spheres. This shell is relatively rigid, and it can prevent

^a Australian Institute for Bioengineering and Nanotechnology, The University of Queensland, Brisbane, QLD 4072, Australia. E-mail: c.yu@uq.edu.au;
Fax: +61 7 3346 3973; Tel: +61 7 3346 3283

^b Materials Engineering, The University of Queensland, Brisbane, QLD 4072, Australia

^c Centre for Microscopy and Microanalysis, The University of Queensland, Brisbane, QLD 4072, Australia

† Electronic supplementary information (ESI) available: Details of experimental procedures, SEM images, TGA curves, N₂ adsorption results, TEM images, XRD patterns, CV curves, and coulombic efficiency. See DOI: 10.1039/c3cc43867h

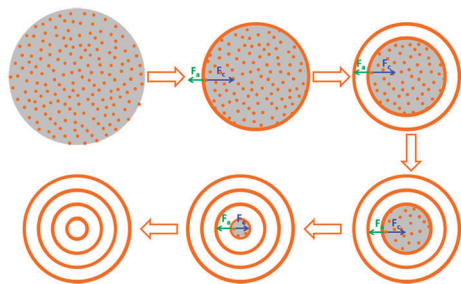


Fig. 1 Schematic illustration for the formation of α -Fe₂O₃ MSHSs.

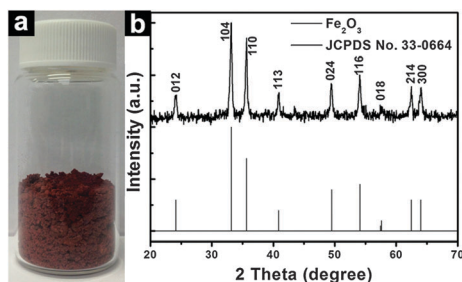


Fig. 2 Digital photograph (a) and the XRD pattern (b) of the α -Fe₂O₃ MSHSs.

the further contraction of the microspheres. Two forces of opposite directions exert at the interface of the composite core and the α -Fe₂O₃ shell. The contraction force (F_c) promotes the inward shrinkage of the core, while the adhesion force (F_a) induces the outward contraction. With a large ΔT , the F_c exceeds F_a , leading to the detachment of the core from the preformed shell. The abovementioned shell formation and core detachment process can be repeated for several times until the ΔT becomes negligible. With a small ΔT , the F_a surpasses F_c , and the mass diffusion trend is reversed. That is, the inner core shrinks outwardly, leaving a cavity at the centre.

Well-developed α -Fe₂O₃ MSHSs can be synthesized on a large scale (Fig. 2a). Fig. 2b is the X-ray diffraction (XRD) pattern and shows that all the diffraction peaks can be well indexed to the rhombohedra α -Fe₂O₃ phase (JCPDS Card No. 33-0664), with a space group of $R\bar{3}c$. No other peaks can be detected, indicating a high purity of the synthesized products. The relatively broad diffraction peaks suggest the nanocrystalline characteristics of the sample. By applying Scherrer equation on the (104) diffraction peak, the average crystallite size can be estimated to be 24 nm.

The morphology and structure of the synthesized products were examined by scanning electron microscopy (SEM) and transmission electron microscopy (TEM). Low-magnification SEM and TEM images show that the synthesized products consist of microspheres with a size of 300–3000 nm (Fig. S3 and S4, ESI[†]). With a low accelerating voltage of 5 kV (Fig. 3a), one can find that the surfaces of the microsphere are not perfectly smooth; instead, wrinkles can be observed on the surface. From the broken part of a microsphere, an inner core particle is exposed, indicating that the microspheres may actually have a yolk-shell or multi-shelled structure. With a high accelerating voltage of 15 kV, the penetration capability of the electrons in SEM can be greatly enhanced, so that the inner cores can be clearly discerned even though the microspheres are intact (Fig. 3b). TEM images as shown in Fig. 3c and d undisputedly demonstrate that the microspheres have a multi-shelled structure and most of the spheres

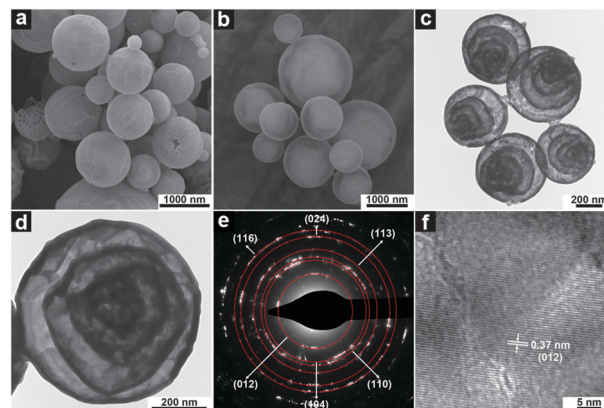


Fig. 3 SEM images (a and b), TEM images (c and d), the SAED pattern (e), and the HRTEM image (f) of α -Fe₂O₃ MSHSs (sample 1).

have four shells. The thickness of the shell is ~ 20 nm, which is generally agreed with the crystallite size determined from XRD. This unique multi-shelled hollow structure gives rise to a surface area of $17.3 \text{ m}^2 \text{ g}^{-1}$ and a pore volume of $0.1 \text{ cm}^3 \text{ g}^{-1}$ (Fig. S5, ESI[†]). Fig. 3e is a selected area electron diffraction (SAED) pattern and shows a series of concentric rings that can be assigned to the {012}, {104}, {110}, {113}, {024} and {116} diffractions of α -Fe₂O₃, respectively. Fig. 3f is a typical high resolution TEM (HRTEM) image, in which the {012} lattice fringes of α -Fe₂O₃ can be clearly observed.

The role of sucrose in the formation of α -Fe₂O₃ MSHSs has been studied (Fig. S6, ESI[†]). The sucrose acts as a matrix, which disperses the iron nitrate and mitigates the hygroscopy of iron nitrate. With a sucrose amount of less than 5 mmol, no iron nitrate–sucrose composite spheres can be formed due to the hygroscopy of the iron nitrate. With an optimised sucrose amount of 7.5–10 mmol, α -Fe₂O₃ MSHSs are obtained (Fig. S6a–c, ESI[†]). With an excess amount of sucrose (more than 15 mmol), α -Fe₂O₃ nanosheets rather than hollow spheres are formed (Fig. S6d–f, ESI[†]).

The effect of the temperature ramp rate has also been investigated. At a low ramp rate of $0.5 \text{ }^\circ\text{C min}^{-1}$, single-shelled hollow spheres and yolk-shell structures are formed (Fig. S7, ESI[†]). At a high ramp rate of 2 and $5 \text{ }^\circ\text{C min}^{-1}$, multi-shelled hollow spheres are obtained (Fig. 3 and Fig. S8, ESI[†]). These results agree well with the heterogeneous contraction mechanism, that is, a lower ramp rate leads to a smaller ΔT , and thus less shells; while a higher ramp rate results in a higher ΔT , and thus more shells.¹²

Besides sucrose, other organic species, such as glucose (Fig. S9a and b, ESI[†]) and polyvinyl alcohol (Fig. S9c and d, ESI[†]) can also be utilized as the matrix to synthesize α -Fe₂O₃ hollow spheres. In addition, this strategy is not limited to the fabrication of α -Fe₂O₃ hollow spheres. As another example, ZnFe₂O₄ yolk-shell structures (Fig. S10 and S11, ESI[†]) can also be fabricated by simply replacing one third of the iron nitrate with zinc nitrate.

To study the lithium storage capabilities of the products, cyclic voltammetry (CV) and galvanostatic charge–discharge cycling were carried out based on the half-cell configuration. The CVs for the initial three cycles at a rate of 0.1 mV s^{-1} are shown in Fig. S12 (ESI[†]). Three cathodic peaks can be observed in the first cycle. The first peak centred at 1.58 V can be attributed to the intercalation of Li⁺ into the crystal structure of α -Fe₂O₃; the second peak centred at 0.93 V can be attributed to the reduction of Fe³⁺ to Fe²⁺; and the

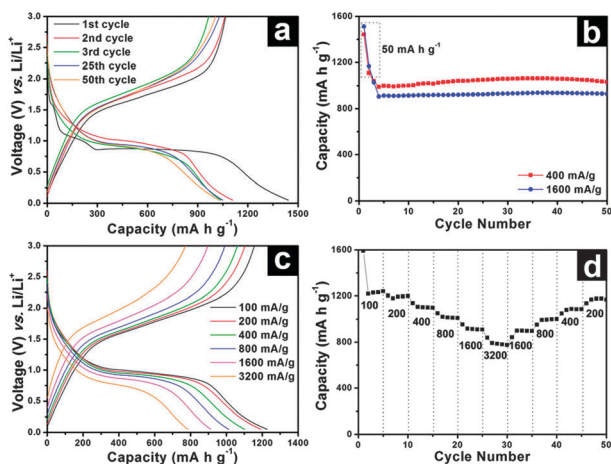


Fig. 4 (a) Charge–discharge profiles at 400 mA g^{-1} ; (b) cycling performance at 400 and 1600 mA g^{-1} ; (c) charge–discharge profiles at current densities of 100 – 3200 mA h g^{-1} ; (d) rate performance of $\alpha\text{-Fe}_2\text{O}_3$ MSHSs.

third peak centred at 0.58 V can be attributed to the reduction of Fe^{2+} to Fe and the irreversible reduction of the electrolyte. In the first anodic process, only one broad peak located between 1.5 and 2.0 V can be observed, corresponding to the oxidation of Fe to Fe^{3+} . From the second cycle onward, a pair of broad cathodic/anodic peaks can be observed and the CV curves generally overlap, suggesting a good reversibility of the redox reaction ($\text{Fe}^{3+} + 3\text{e}^- \leftrightarrow \text{Fe}$).

The cycling performance of the $\alpha\text{-Fe}_2\text{O}_3$ MSHSs was evaluated by activating the half cells at 50 mA g^{-1} for two cycles and then cycling at 400 or 1600 mA g^{-1} . At a current of 50 mA g^{-1} , the $\alpha\text{-Fe}_2\text{O}_3$ MSHSs delivers an initial discharge capacity of 1443 mA h g^{-1} and a charge capacity of 1067 mA h g^{-1} , respectively (Fig. 4a).

After the activation process, a high and stable capacity of ~ 1000 and 900 mA h g^{-1} can be achieved at a current of 400 and 1600 mA g^{-1} , respectively, as shown in Fig. 4b. The coulombic efficiency for the first cycle is around 75% , while it stabilizes at $\sim 98\%$ after the activation process (Fig. S13, ESI[†]).

The rate performance of the $\alpha\text{-Fe}_2\text{O}_3$ was also investigated by cycling the material at various currents ranging from 100 to 3200 mA g^{-1} . Fig. 4c shows representative charge–discharge profiles (the third cycle at each rate). As the current density increases from 100 to 200 , 400 , 800 , 1600 and 3200 mA g^{-1} , the capacity only decreases slightly from 1228 to 1193 , 1102 , 1013 , 913 and 784 mA h g^{-1} (Fig. 4c and d), indicating the excellent rate capability of the $\alpha\text{-Fe}_2\text{O}_3$ MSHSs. After reaching its highest value, that is 3200 mA g^{-1} , the current density is reduced to 200 mA g^{-1} gradually. A capacity of 1176 mA h g^{-1} can be recovered at 200 mA g^{-1} , which is 98.6% of the capacity at the same current density before the high rate measurement. The obtained capacity exceeds the theoretical value for Fe_2O_3 . This phenomenon has also been observed in other conversion reaction-based anodes, and can be attributed to the reversible formation/dissolution of polymeric layers on the surface of electrodes.¹³

Notably, the electrochemical performances of the $\alpha\text{-Fe}_2\text{O}_3$ MSHSs are superior or at least comparable to those of state-of-the-art Fe_2O_3 -based anode materials reported recently, such as nanorods,^{9b} hollow spheres,^{10a,b} Fe_2O_3 -carbon nanotubes^{11a–d} and Fe_2O_3 -reduced graphene oxide.^{11e} The enhanced performances can be attributed to the unique structural characteristics of the $\alpha\text{-Fe}_2\text{O}_3$ MSHSs.

The permeable and thin shells greatly shorten the distances for Li^+ diffusion; the void space effectively accommodates the dramatic volume change and alleviates the strain during lithiation–delithiation. All these features contribute to the high electrochemical performance. The TEM study shows that the multi-shelled spherical structure can be well retained after the first discharge–charge cycle (Fig. S14, ESI[†]), and partially preserved after 50 cycles (Fig. S15, ESI[†]), indicating that these desirable features can be maintained during lithiation–delithiation.

In conclusion, a facile method has been developed for the continuous and scalable production of $\alpha\text{-Fe}_2\text{O}_3$ MSHSs. The resultant material delivers a high specific reversible capacity of $\sim 1200 \text{ mA h g}^{-1}$ with good cycling stability and excellent rate capability. It is expected that the present strategy could be extended to the fabrication of various metal oxide hollow structures for a broad spectrum of applications such as LIBs, catalysis, photocatalysis, and gas sensing.

The authors acknowledge the Australian Research Council for financial support. L.Z. gratefully acknowledges the award of The University of Queensland Postdoctoral Research Fellowship. The Australian Microscopy & Microanalysis Research Facility and Australian National Fabrication Facility are acknowledged for providing structural characterization facilities.

Notes and references

- (a) F. Caruso, R. A. Caruso and H. Mohwald, *Science*, 1998, **282**, 1111; (b) Y. D. Yin, R. M. Rioux, C. K. Erdonmez, S. Hughes, G. A. Somorjai and A. P. Alivisatos, *Science*, 2004, **304**, 711; (c) X. W. Lou, L. A. Archer and Z. C. Yang, *Adv. Mater.*, 2008, **20**, 3987.
- (a) X. Y. Lai, J. E. Halpert and D. Wang, *Energy Environ. Sci.*, 2012, **5**, 5604; (b) W. Cho, Y. H. Lee, H. J. Lee and M. Oh, *Adv. Mater.*, 2011, **23**, 1720; (c) L. Zhou, D. Y. Zhao and X. W. Lou, *Adv. Mater.*, 2012, **24**, 745; (d) G. Q. Zhang, L. Yu, H. B. Wu, H. E. Hoster and X. W. Lou, *Adv. Mater.*, 2012, **24**, 4609; (e) Y. J. Hong, M. Y. Son and Y. C. Kang, *Adv. Mater.*, 2013, **25**, 2279.
- M. Yang, J. Ma, C. L. Zhang, Z. Z. Yang and Y. F. Lu, *Angew. Chem., Int. Ed.*, 2005, **44**, 6727.
- X. W. Lou, C. L. Yuan and L. A. Archer, *Small*, 2007, **3**, 261.
- (a) Z. H. Dong, X. Y. Lai, J. E. Halpert, N. L. Yang, L. X. Yi, J. Zhai, D. Wang, Z. Y. Tang and L. Jiang, *Adv. Mater.*, 2012, **24**, 1046; (b) X. Y. Lai, J. Li, B. A. Korgel, Z. H. Dong, Z. M. Li, F. B. Su, J. A. Du and D. Wang, *Angew. Chem., Int. Ed.*, 2011, **50**, 2738.
- Z. Y. Wang, D. Y. Luan, C. M. Li, F. B. Su, S. Madhavi, F. Y. C. Boey and X. W. Lou, *J. Am. Chem. Soc.*, 2010, **132**, 16271.
- (a) X. Wang, X. L. Wu, Y. G. Guo, Y. T. Zhong, X. Q. Cao, Y. Ma and J. N. Yao, *Adv. Funct. Mater.*, 2010, **20**, 1680; (b) H. L. Xu and W. Z. Wang, *Angew. Chem., Int. Ed.*, 2007, **46**, 1489.
- Y. Zeng, X. Wang, H. Wang, Y. Dong, Y. Ma and J. N. Yao, *Chem. Commun.*, 2010, **46**, 4312.
- (a) J. Chen, L. N. Xu, W. Y. Li and X. L. Gou, *Adv. Mater.*, 2005, **17**, 582; (b) Y. M. Lin, P. R. Abel, A. Heller and C. B. Mullins, *J. Phys. Chem. Lett.*, 2011, **2**, 2885.
- (a) S. L. Chou, J. Z. Wang, D. Wexler, K. Konstantinov, C. Zhong, H. K. Liu and S. X. Dou, *J. Mater. Chem.*, 2010, **20**, 2092; (b) B. Wang, J. S. Chen, H. B. Wu, Z. Y. Wang and X. W. Lou, *J. Am. Chem. Soc.*, 2011, **133**, 17146; (c) L. Zhang, H. B. Wu, S. Madhavi, H. H. Hng and X. W. Lou, *J. Am. Chem. Soc.*, 2012, **134**, 17388.
- (a) W. J. Yu, P. X. Hou, L. L. Zhang, F. Li, C. Liu and H. M. Cheng, *Chem. Commun.*, 2010, **46**, 8576; (b) W. J. Yu, P. X. Hou, F. Li and C. Liu, *J. Mater. Chem.*, 2012, **22**, 13756; (c) G. M. Zhou, D. W. Wang, P. X. Hou, W. S. Li, N. Li, C. Liu, F. Li and H. M. Cheng, *J. Mater. Chem.*, 2012, **22**, 17942; (d) Z. Y. Wang, D. Y. Luan, S. Madhavi, Y. Hu and X. W. Lou, *Energy Environ. Sci.*, 2012, **5**, 5252; (e) X. J. Zhu, Y. W. Zhu, S. Murali, M. D. Stollers and R. S. Ruoff, *ACS Nano*, 2011, **5**, 3333.
- J. G. Guan, F. Z. Mou, Z. G. Sun and W. D. Shi, *Chem. Commun.*, 2010, **46**, 6605.
- K. M. Shaju, F. Jiao, A. Debart and P. G. Bruce, *Phys. Chem. Chem. Phys.*, 2007, **9**, 1837.

Electronic Supplementary Information (ESI)

Experimental

Materials Synthesis: The α -Fe₂O₃ MSHSs hollow microspheres were prepared by a spray drying method followed by annealing in air. In a typical synthesis (Sample 1, see Table S1), Fe(NO₃)₃·9H₂O (10 mmol) and sucrose (10 mmol) were dissolved in H₂O (100 mL) to form a clear solution. The resulting solution was then spray dried using a Buchi mini spray drier B-290 at an inlet temperature of 220 °C, an aspirator rate of 100 %, a rotameter setting of 60 mm, and a pump rate of 5 % (1.5 mL/min). Nitrogen was used as the drying gas. These settings resulted in an outlet temperature of ~ 130 °C. The spray dried samples (iron nitrate-sucrose composite) were then annealed in air at 400 °C for 5 hours with a temperature ramp rate of 2 °C/min. To study the influence of synthesis parameters on the structures, a series of samples were prepared by adjusting the feeding ratio of reagents, the temperature ramp rate, and the choices of organic matrices. The detailed synthesis conditions for all samples are listed in Table S1.

Characterization: XRD patterns were collected on a German Bruker D8 Advanced X-Ray Diffractometer with Ni filtered Cu K α radiation (40 kV, 30 mA). Field emission SEM images were obtained on a JEOL JSM 7800 with accelerating voltages of 5.0 and 15.0 kV, respectively, while TEM images were taken on Philips Tecnai F20 (operated at 200 kV). Thermo gravimetric analysis (TGA) was carried out on a TGA/DSC1 STAR^e System under air flow (25 – 1000 °C, 5 °C/min). Nitrogen adsorption isotherms were measured at 77 K using a TriStar II Surface Area and Porosity analyser (Micromeritics). The samples were degassed under vacuum for 6 hours at 200 °C before analysis. BET surface area was calculated from the adsorption branch in relative pressure (p/p₀) range of 0.05 – 0.30.

Electrochemical Measurement: The electrochemical measurements were carried out in homemade two-electrode Swagelok type cells. The working electrode is consisted of active material, conductive acetylene black, and polyvinylidene fluoride binder in a weight ratio of 70:20:10. Lithium chips were used as both the counter electrode and reference electrode. 1 M LiPF₆ in a mixture of ethylene carbonate, dimethyl carbonate, and diethyl carbonate (1:1:1 in volume) was used as the electrolyte. Cell assembly was carried out in an Ar-filled glovebox with moisture and oxygen concentrations below 1.0 ppm. CV measurements were performed on a Solartron 1480 MultiStat instrument. The galvanostatic charge-discharge tests were performed on a MTI 8 Channels Battery Analyzer.

Table 1. Synthesis conditions for α -Fe₂O₃ hollow structures/nanostructures.

Sample Name	Organic Species	Iron Nitrate	Temperature ramp rate
Sample 1	Sucrose, 10 mmol	10 mmol	2 °C/min
Sample 2	Sucrose, 7.5 mmol	10 mmol	2 °C/min
Sample 3	Sucrose, 15 mmol	10 mmol	2 °C/min
Sample 4	Sucrose, 20 mmol	10 mmol	2 °C/min
Sample 5	Sucrose, 10 mmol	10 mmol	0.5 °C/min
Sample 6	Sucrose, 10 mmol	10 mmol	5 °C/min
Sample 7	Glucose, 20 mmol	10 mmol	2 °C/min
Sample 8	PVA, ^a 4 g	10 mmol	2 °C/min

a PVA: polyvinyl alcohol

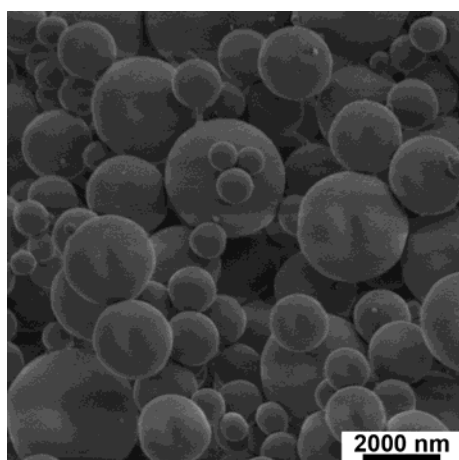


Figure S1. FESEM images of iron nitrate-sucrose composite microspheres (sucrose/iron nitrate ratio: 10/10).

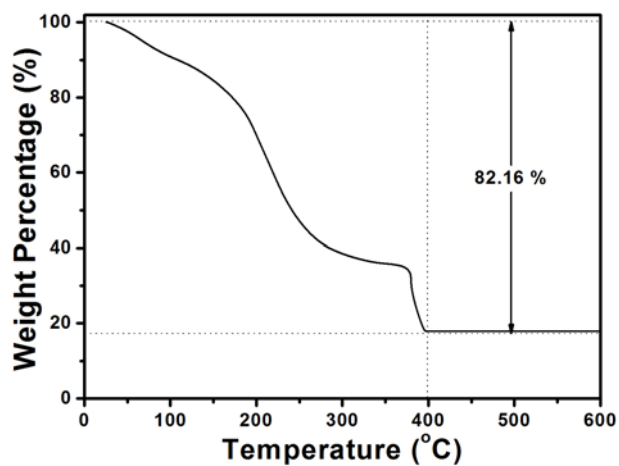


Figure S2. TGA curve of the iron nitrate-sucrose composites (sucrose/iron nitrate ratio: 10/10).

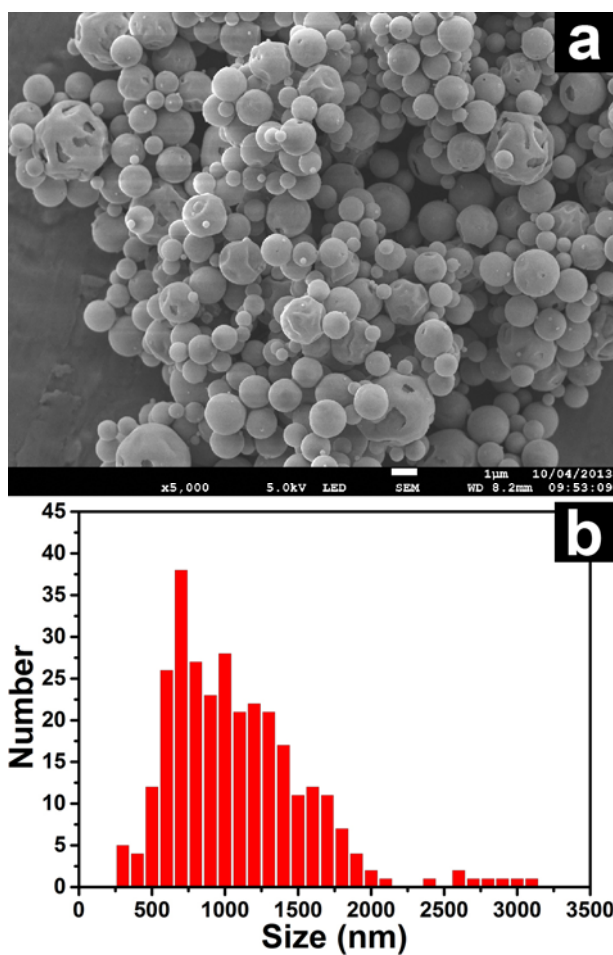


Figure S3. Low-magnification SEM image and the corresponding particle size distribution of α - Fe_2O_3 MSHSs.

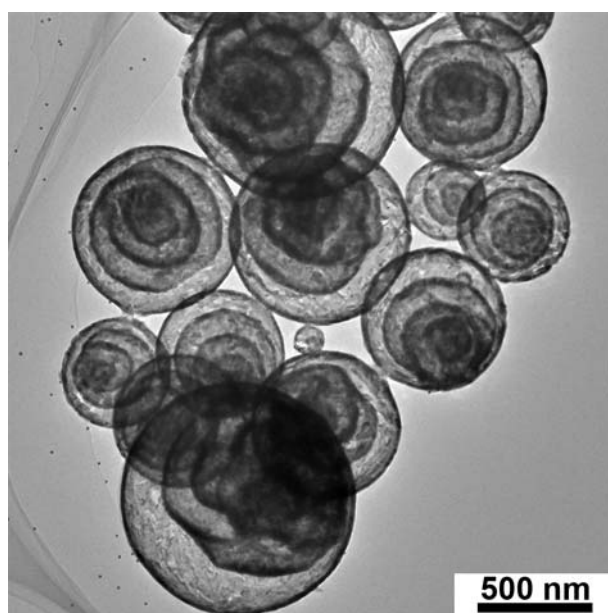


Figure S4. Low-magnification TEM image of α -Fe₂O₃ MSHSs.

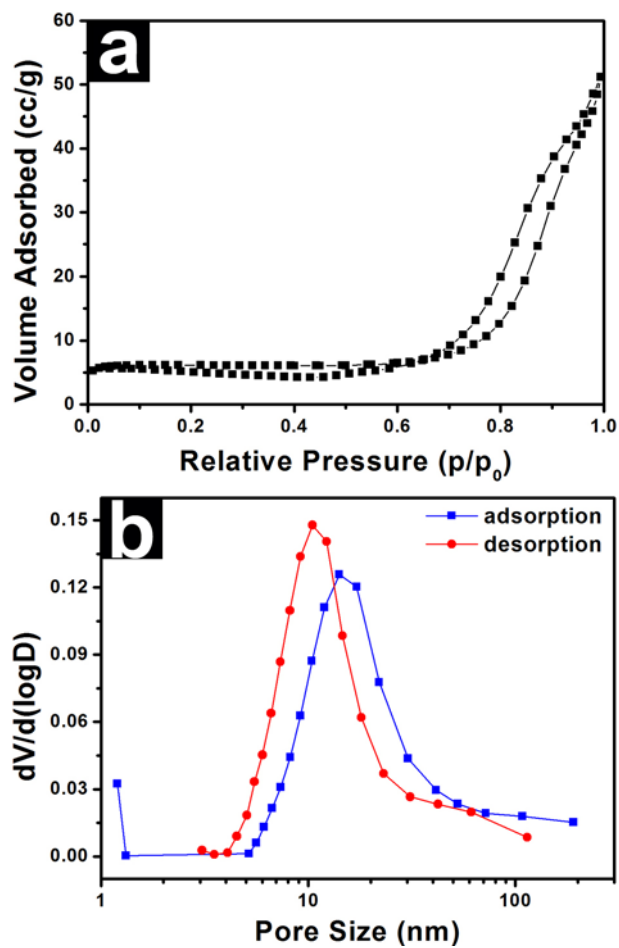


Figure S5. Nitrogen adsorption isotherm (a) and pore size distributions (b) of the α - Fe_2O_3 MSHSs (Sample 1).

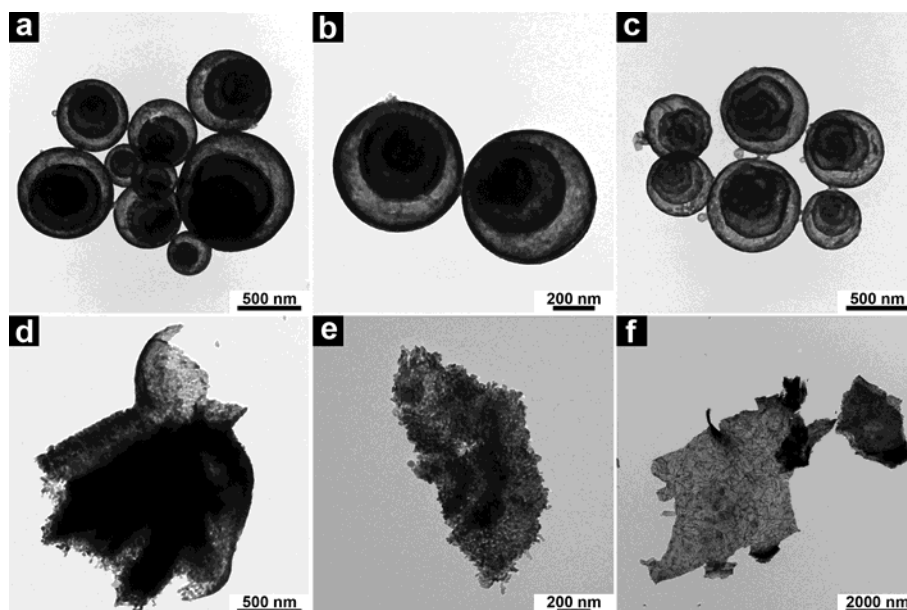


Figure S6. TEM images of Sample 2 (a and b, sucrose/iron nitrate ratio: 7.5/10), Sample 1 (c, sucrose/iron nitrate ratio: 10/10), Sample 3 (d and e, sucrose/iron nitrate ratio: 15/10), and Sample 4 (f, sucrose/iron nitrate: 20/10).

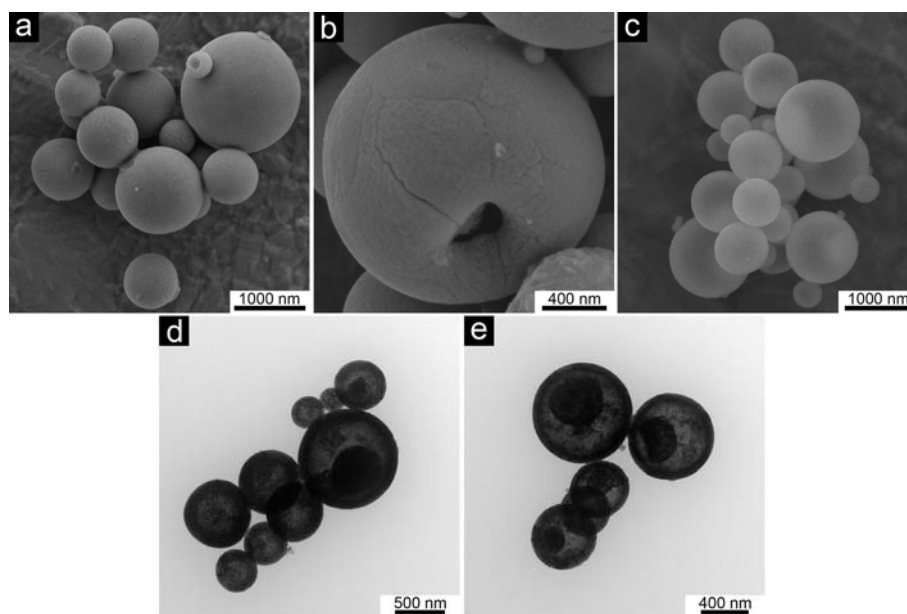


Figure S7. FESEM (a – c) and TEM (d, e) images of α -Fe₂O₃ hollow structures (Sample 5, temperate ramp rate: 0.5 °C/min). For a and b, the accelerating voltage is 5 kV; for c, the accelerating voltage is 15 kV.

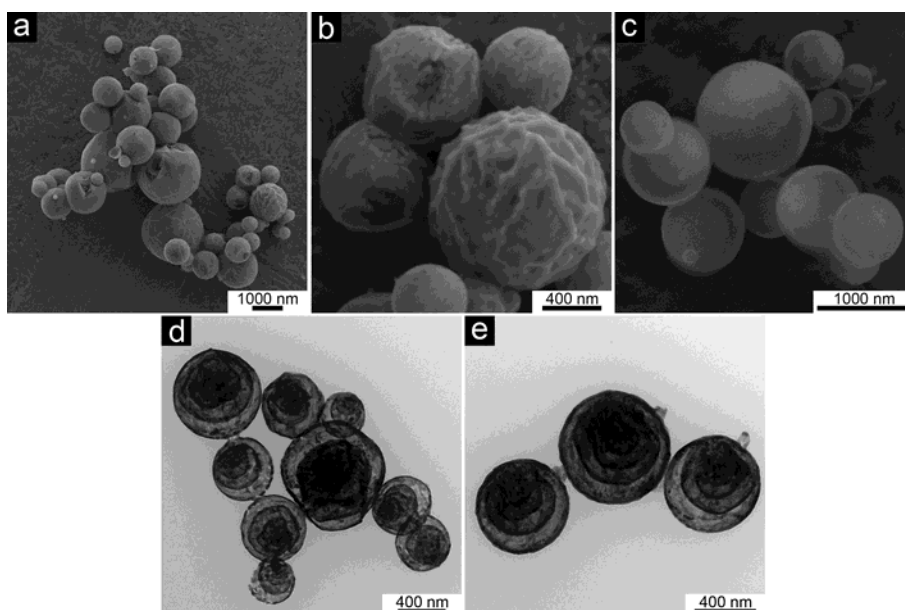


Figure S8. FESEM (a – c) and TEM (d, e) images of α -Fe₂O₃ hollow structures (Sample 6, temperature ramp rate: 5 °C/min). For a and b, the accelerating voltage is 5 kV; for c, the accelerating voltage is 15 kV.

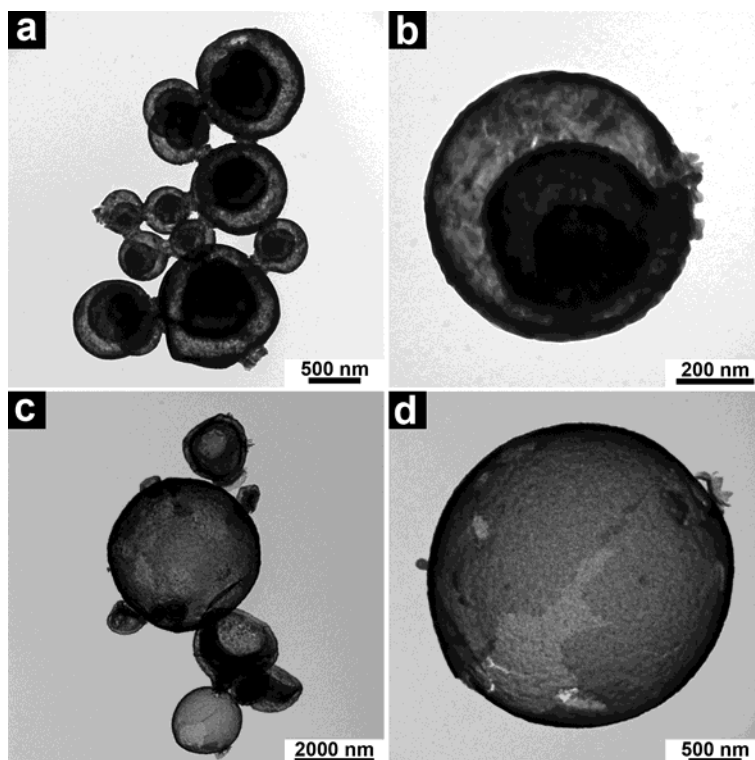


Figure S9. TEM images of α -Fe₂O₃ hollow structures using glucose (a and b, Sample 7) and PVA (c and d, Sample 8) as the organic species.

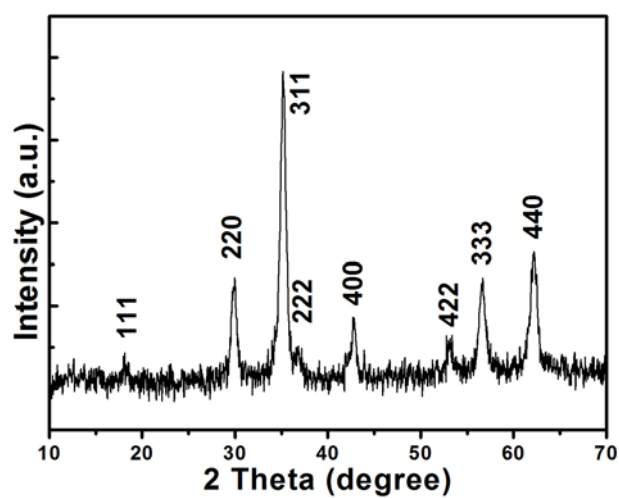


Figure S10. XRD pattern of the ZnFe_2O_4 yolk-shell structures.

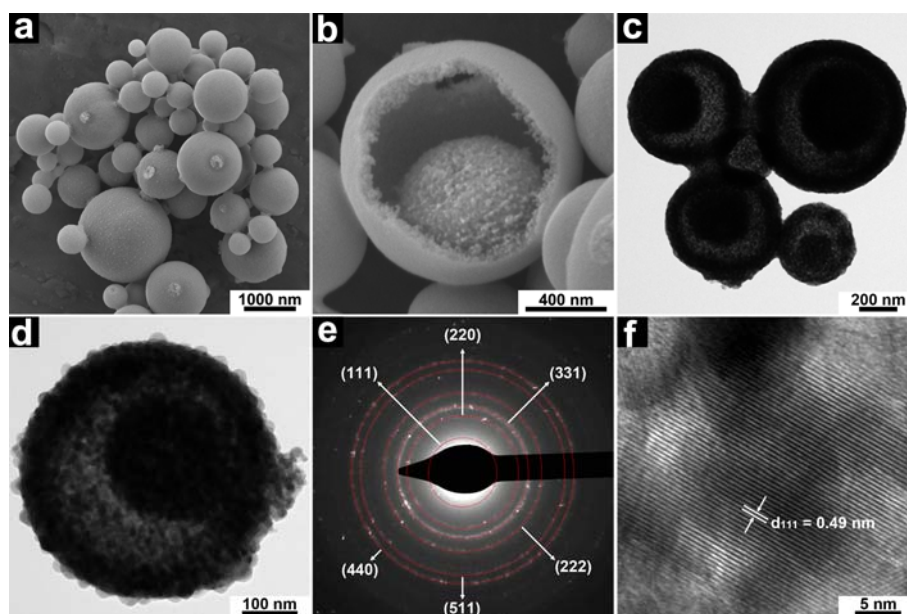


Figure S11. FESEM (a, b), TEM (c, d), SAED (e) and HRTEM (f) images of ZnFe_2O_4 yolk-shell structures.

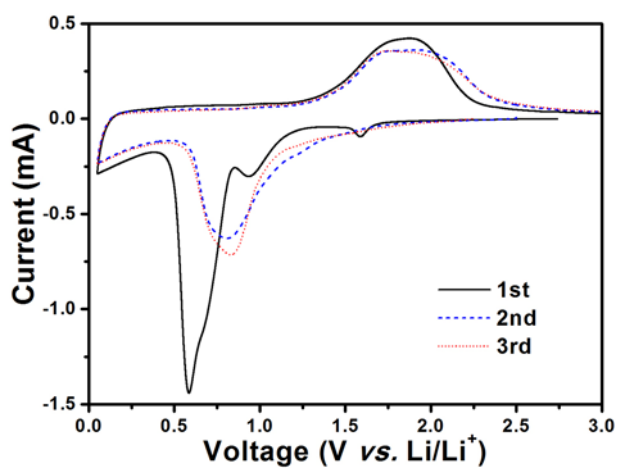


Figure S12. CVs of α -Fe₂O₃ MSHSs for the initial three cycles at a rate of 0.1 mA s⁻¹.

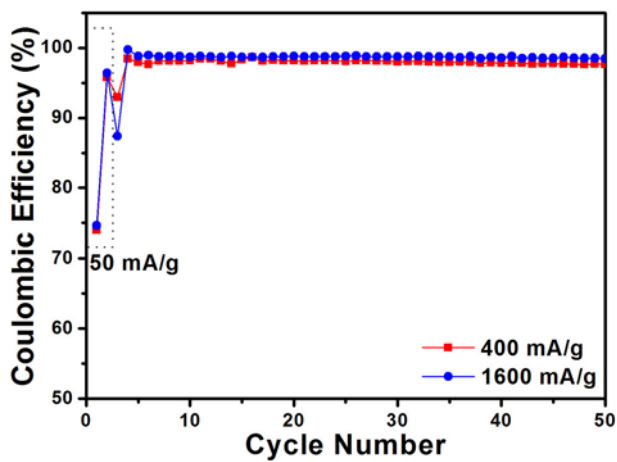


Figure S13. Coulombic efficiency vs. cycle number.

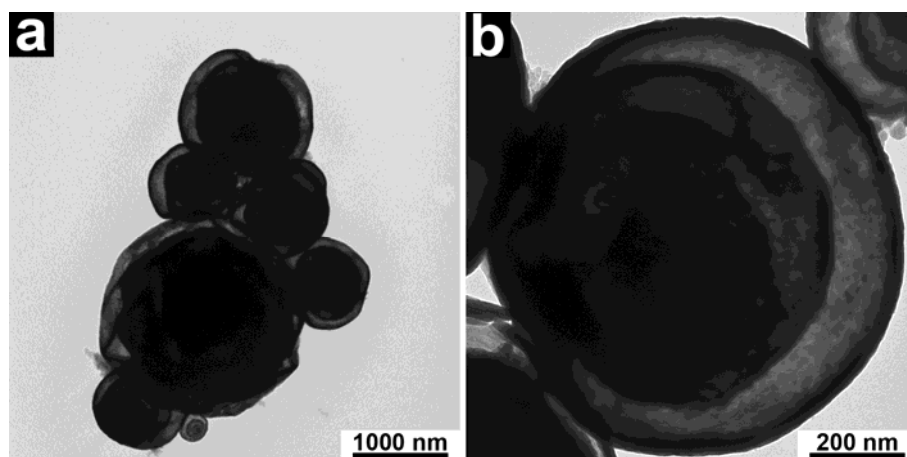


Figure S14. TEM images of the α -Fe₂O₃ MSHSs after the first discharge-charge cycle at 400 mA g⁻¹.

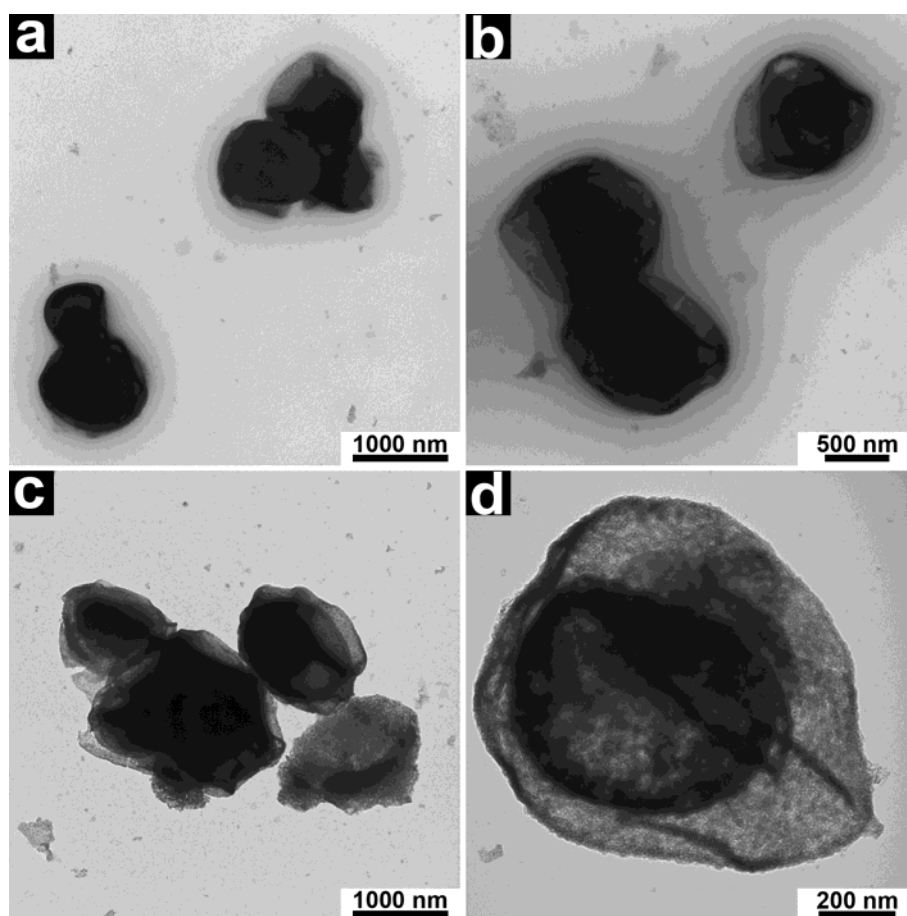


Figure S15. TEM images of the α -Fe₂O₃ MSHSs after 50 discharge-charge cycles at 400 mA g⁻¹.